Mon. Not. R. Astron. Soc. **353,** 732–746 (2004) doi:10.1111/j.1365-2966.2004.08206.x

High-sensitivity measurements of the cosmic microwave background power spectrum with the extended Very Small Array

Clive Dickinson,[1]★† Richard A. Battye,[1] Pedro Carreira,[1] Kieran Cleary,[1] Rod D. Davies,[1] Richard J. Davis,[1] Ricardo Genova-Santos,[2] Keith Grainge,[3] Carlos M. Gutiérrez,[2] Yaser A. Hafez,[1] Michael P. Hobson,[3] Michael E. Jones,[3] Rüdiger Kneissl,[3] Katy Lancaster,[3] Anthony Lasenby,[3] J. P. Leahy,[1] Klaus Maisinger,[3] Carolina Ödman,[3] Guy Pooley,[3] Nutan Rajguru,[3] Rafael Rebolo,[2,4] José Alberto Rubiño-Martin,[2]‡ Richard D. E. Saunders,[3] Richard S. Savage,[3]§ Anna Scaife,[3] Paul F. Scott,[3] Anže Slosar,[3]¶ Pedro Sosa Molina,[2] Angela C. Taylor,[3] David Titterington,[3] Elizabeth Waldram,[3] Robert A. Watson[1]‖ and Althea Wilkinson[1]

[1]*Jodrell Bank Observatory, University of Manchester, Macclesfield, Cheshire SK11 9DL*
[2]*Instituto de Astrofisíca de Canarias, 38200 La Laguna, Tenerife, Canary Islands, Spain*
[3]*Astrophysics Group, Cavendish Laboratory, University of Cambridge, Madingley Road, Cambridge CB3 0HE*
[4]*Consejo Superior de Investigaciones Cientificas, Spain*

Accepted 2004 July 7. Received 2004 June 30; in original form 2004 February 23

ABSTRACT

We present deep *Ka*-band ($\nu \approx 33$ GHz) observations of the cosmic microwave background (CMB) made with the extended Very Small Array (VSA). This configuration produces a naturally weighted synthesized FWHM beamwidth of ∼11 arcmin, which covers an ℓ range of 300 to 1500. On these scales, foreground extragalactic sources can be a major source of contamination to the CMB anisotropy. This problem has been alleviated by identifying sources at 15 GHz with the Ryle Telescope and then monitoring these sources at 33 GHz using a single-baseline interferometer collocated with the VSA. Sources with flux densities $\gtrsim$20 mJy at 33 GHz are subtracted from the data. In addition, we calculate a statistical correction for the small residual contribution from weaker sources that are below the detection limit of the survey.

The CMB power spectrum corrected for Galactic foregrounds and extragalactic point sources is presented. A total ℓ range of 150–1500 is achieved by combining the complete extended array data with earlier VSA data in a compact configuration. Our resolution of $\Delta\ell \approx 60$ allows the first three acoustic peaks to be clearly delineated. This is achieved by using mosaiced observations in seven regions covering a total area of 82 deg^2. There is good agreement with the *Wilkinson Microwave Anisotropy Probe* (*WMAP*) data up to $\ell = 700$ where *WMAP* data run out of resolution. For higher ℓ values out to $\ell = 1500$, the agreement in power spectrum amplitudes with other experiments is also very good despite differences in frequency and observing technique.

Key words: techniques: interferometric – cosmic microwave background – cosmology: observations.

1 INTRODUCTION

The angular power spectrum of primordial anisotropies in the cosmic microwave background (CMB) has become an important tool

★E-mail: cdickins@jb.man.ac.uk
†Present address: California Institute of Technology, Mail Stop 105-24, 1200 E. California Boulevard, Pasadena, CA 91125, USA.
‡Present address: Max-Planck Institut für Astrophysik, Karl-Schwazchild-Str. 1, Postfach 1317, 85741 Garching, Germany.
§Present address: Astronomy Centre, University of Sussex, Falmer, Brighton BN1 9QH.
¶Present address: Faculty of Mathematics & Physics, University of Ljubljana, 1000 Ljubljana, Slovenia.
‖Present address: Instituto de Astrofísica de Canarias, 38200 La Laguna, Tenerife, Spain.

in the era of precision cosmology. Because the first statistical detection of CMB fluctuations on large angular scales ($\ell = 2$–30) by the *COBE*-Differential Microwave Radiometer (DMR) instrument (Smoot et al. 1992), several experiments have detected acoustic peaks in the power spectrum in the ℓ range 100–1000 (Lee et al. 2001; Halverson et al. 2002; Netterfield et al. 2002; Benoît et al. 2003; Scott et al. 2003, hereafter Paper III) and a fall-off in power at high ℓ values (Dawson et al. 2002; Grainge et al. 2003; Kuo et al. 2004; Readhead et al. 2004). More recently, the *Wilkinson Microwave Anisotropy Probe* (*WMAP*) has provided unprecedented measurements over the ℓ range 2–700 (Bennett et al. 2003a; Hinshaw 2003a). The *WMAP* 1-yr power spectrum is cosmic variance limited up to $\ell = 350$ and delineates the first two peaks at $\ell \sim 220$ and 550 with exceptional signal-to-noise ratios. The new data have provided detailed cosmological information on a wide range of parameters (Spergel et al. 2003) and have raised new questions to be answered. However, the angular resolution of *WMAP* limits the power spectrum to $\ell \lesssim 800$. At high-ℓ values, the origin of the excess power initially observed by the Cosmic Background Imager (CBI) at $\ell = 2000$–4000 (Mason et al. 2003) has also generated much interest. It is clear that the high-ℓ CMB power spectrum is one of the challenges for future CMB experiments including the ESA *Planck* satellite (Tauber 2001; Lawrence 2003) due for launch in 2007.

The Very Small Array (VSA) (Watson et al. 2003, hereafter Paper I) is a purpose-built radio interferometer that has measured the CMB angular power spectrum between $\ell = 150$ and 900 in a compact array configuration (Paper III) and more recently up to $\ell = 1400$ in an extended array (Grainge et al. 2003). This paper describes the complete set of extended array data observed during 2001 October—2003 June. The data cover a larger area of sky than those analysed by Grainge et al. (2003) by adding more pointings to the previous VSA fields and by observing four new fields. We use mosaicing techniques to increase the sensitivity, reduce the sample variance and to facilitate finer ℓ resolution, or equivalently reduce correlations between ℓ bins, over the range $\ell = 300$–1500.

The paper is organized as follows. Section 2 summarizes the telescope parameters and the extended array configuration. In Section 3 we describe the observations, data reduction and calibration of the data, including a range of data checks. In Section 4 we discuss the various foregrounds, particularly discrete radio sources, and the corrections that were made to the data. The main results, CMB mosaic maps and CMB power spectrum covering $\ell = 150$–1500, are presented in Section 5. A morphological analysis of the power spectrum is given in Section 5.3. Section 6 is a discussion of the results and comparisons with other data, followed by conclusions in Section 7. The cosmological interpretation of these data, both on their own and combined with other data, is described in a companion paper (Rebolo et al. 2004).

2 THE VSA EXTENDED ARRAY

The VSA is a 14-element interferometer operating in the *Ka* band (26–36 GHz) situated at the high and dry site of the El Teide observatory, in Tenerife, at an altitude of 2340 m (see Paper I). Each antenna comprises a conical corrugated horn feeding a paraboloid mirror and mounted anywhere on a 4×3 m^2 tip-tilt table located in a metal enclosure to minimize ground emission. As a result of the geometry of the table and enclosure, the VSA declination range is restricted to -5° to $+60^\circ$. In the compact configuration (Taylor et al. 2003, hereafter Paper II), the mirrors were 143 mm in diameter giving a primary beam of $4\overset{\circ}{.}6$ FWHM at 34 GHz. The extended array, described here, has larger 322-mm-diameter apertures allowing longer baselines while maintaining a high filling factor and therefore high temperature sensitivity. The longer baselines increase the angular resolution while the larger horns give a primary beam of $2\overset{\circ}{.}1$ FWHM at 33 GHz. This configuration has a total of 91 baselines with lengths ranging from 0.6 to 2.5 m as shown in Fig. 1. The maximum possible baseline length, set by the extent of the main tip-tilt table, is considerably higher with lengths up to ∼4 m. However, for the data presented here, we chose a limited range of lengths to maximize the overall temperature sensitivity of the array.[1] This still allows a wide range of angular scales to be measured but with well-sampled u, v coverage (Fig. 1), which in turn provides good sampling of the power spectrum in ℓ and mapping with high fidelity. The filling factor of this configuration is ∼1.6 times greater than that of the compact array, leading to an increase in the overall temperature sensitivity of the array.

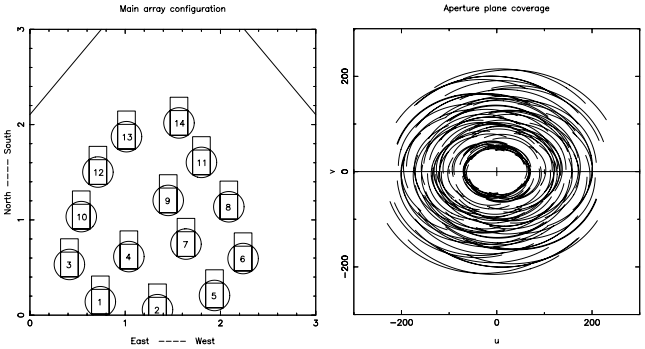

Figure 1. Left panel: the extended array configuration of 14 antennas on the tip-tilt table. Right panel: the corresponding u, v coverage (units of wavelengths) for a 5-h observation at declination $+40^\circ$.

The VSA has so far operated in a single channel with instantaneous bandwidth of 1.5 GHz. We chose to use the higher end of the band (∼33 GHz) to minimize foregrounds because the minimum contamination for total-power measurements is at ∼70 GHz (Banday et al. 2003; Bennett et al. 2003b). With an average system temperature of ∼35 K, the VSA achieves an overall instantaneous point-source sensitivity of ~ 6 Jy s$^{-1/2}$. This corresponds to a temperature sensitivity, over a synthesized beam area ($\Omega_{\rm synth} \approx 1 \times 10^{-5}$ sr) of ~ 15 mK s$^{-1/2}$. Note that the exact conversion from flux density to temperature depends on the beam area and on the u, v coverage, which in turns depends on the declination and the flagging/filtering of the visibility data. A typical VSA field at declination 40° gives a total ℓ range of ∼300–1500 and a naturally weighted synthesized beam of FWHM ∼11 arcmin over a $\sim 2\overset{\circ}{.}1$ field-of-view. The specifications for the VSA extended array are summarized in Table 1.

3 OBSERVATIONS AND DATA REDUCTION

3.1 Observations

The observations presented in this paper were made during the period 2001 October—2003 July with the array configuration described in Section 2. They consist of a total of 33 pointings that make up three seven-field mosaics (VSA1, VSA2, VSA3) and four three-field mosaics (VSA5, VSA6, VSA7, VSA8) giving a total area coverage of 82 deg^2. The sky positions for these seven regions are

[1] The maximum baseline lengths possible with the current tip-tilt table, corresponding to $\ell \sim 2500$, will be utilized in future CMB observations with the VSA.

Table 1. Specifications of the VSA in the extended array configuration.

Location	Izana, Tenerife (2340 m)
Latitude	$+28^\circ 18'$
Declination range	$-5^\circ <$ Dec. $< +60^\circ$
No. of antennas (baselines)	14 (91)
Range of baseline lengths	0.6–2.5 m
Centre frequencies	33, 34 GHz
Bandwidth, $\Delta\nu$	1.5 GHz
System temperature, $T_{\rm sys}$ (K)	$\sim$35 K
Mirror diameters	322 mm
Primary beam	2.°1 FWHM at 33 GHz
Synthesized beam (FWHM)	$\approx$11 arcmin
Range of ℓ	$\sim$300–1500
Point-source flux sensitivity	$\sim$6 Jy s$^{-1/2}$
Temperature sensitivity	$\sim$15 mK s$^{-1/2}$

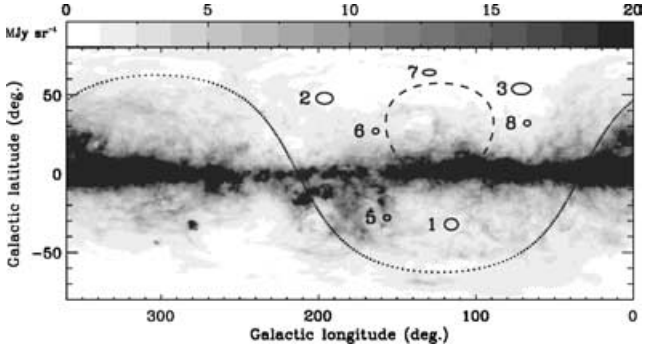

Figure 2. All-sky 100-μm map (SFD98) in Galactic coordinates. The greyscale is linear from 0 to 20 MJy sr^{-1}. The locations of the seven VSA regions are shown as circles, stretched in the horizontal direction as a result of the map projection, with diameters scaled up for clarity. The larger ellipses are the seven-field regions, labelled 1, 2 and 3, and the smaller ellipses, labelled 5, 6, 7 and 8, are the three-field regions. The dashed and dotted lines indicate the declination limits for the VSA at $+60^\circ$ and -5°, respectively.

depicted in Fig. 2 superposed on the 100 μm all-sky map based on Diffuse Infrared Background Experiment (DIRBE)/*IRAS* data (Schlegel, Finkbeiner & Davis 1998, henceforth SFD98) in Galactic coordinates. The field centres and approximate integration times are listed in Table 2. The total effective integration time is $\approx$6000 h (250 d) after filtering and flagging of the data.

The fields were carefully chosen to minimize Galactic and extragalactic emission. This includes avoiding bright galaxy clusters based on existing catalogues (Abell 1958; Ebeling et al. 1998) and bright radio sources ($\gtrsim$500 mJy) based on the NRAO VLA Sky Survey (NVSS) 1.4-GHz survey (Condon et al. 1998) and GB6 survey at 4.85 GHz (Gregory et al. 1996). Avoiding galaxy clusters is important as a result of the potential for Sunyaev–Zel'dovich (SZ) effect decrements to contaminate VSA data (see Section 4.3). Diffuse Galactic emission is minimized by choosing fields with low emission as predicted by templates of synchrotron, free–free and dust emission (see Section 4.2); all fields are at Galactic latitudes $|b| \gtrsim 27^\circ$. The VSA regions are distributed evenly in right ascension to optimize for 24-h observations. Each field is observed on a daily basis for up to a maximum of 5 h. Where possible, observations are centred on transit to minimize ground spillover and system temperatures, giving a maximum hour angle range of $\pm$2.5 h. Calibrator observations of several bright radio sources were interleaved between fields for typically 10 min–1 h to provide flux and phase calibrations (Section 3.3). At the same time as the VSA, a single-baseline interferometer monitors the brightest sources in the same patch of sky as part of the source-subtraction process described in more detail in Section 4.1.

Table 2. Celestial (J2000) coordinates for each of the 33 fields observed by the VSA in the extended array. The effective integration time is calculated after flagging and filtering of the data. VSA1, VSA2 and VSA3 are seven-field mosaics and VSA5, VSA6, VSA7 and VSA8 are three-field mosaics giving a total of 33 pointings.

	RA (J2000)	Dec. (J2000)	$t_{\rm int}$ (h)
VSA1E	$00^{\rm h}22^{\rm m}37^{\rm s}$	$+30^\circ 16^{\rm m}38^{\rm s}$	126
VSA1F	00 16 52	+30 24 10	118
VSA1G	00 19 22	+29 16 39	112
VSA1H	00 25 04	+29 09 07	142
VSA1J	00 13 40	+29 24 11	184
VSA1K	00 21 47	+28 09 08	207
VSA1L	00 16 09	+28 16 40	315
VSA2E	09 37 57	+30 41 28	131
VSA2F	09 43 46	+30 41 14	120
VSA2G	09 40 53	+31 46 21	165
VSA2H	09 35 00	+31 46 36	308
VSA2J	09 46 46	+31 46 06	214
VSA2K	09 37 55	+32 51 28	181
VSA2L	09 43 52	+32 51 13	253
VSA3E	15 31 43	+43 49 53	172
VSA3F	15 38 38	+43 50 18	124
VSA3G	15 35 13	+42 45 05	154
VSA3H	15 28 25	+42 44 42	213
VSA3J	15 42 02	+42 45 30	239
VSA3K	15 31 53	+41 39 54	164
VSA3L	15 38 35	+41 40 17	332
VSA5E	03 02 57	+26 11 44	196
VSA5F	03 08 32	+26 11 26	173
VSA5G	03 05 45	+27 16 35	216
VSA6E	07 28 59	+53 53 49	56
VSA6F	07 20 30	+53 54 23	141
VSA6G	07 24 48	+55 05 00	203
VSA7E	12 32 22	+52 43 27	73
VSA7F	12 24 07	+52 43 23	153
VSA7G	12 28 14	+53 48 25	206
VSA8E	17 31 34	+41 57 53	187
VSA8F	17 38 18	+41 58 22	300
VSA8G	17 34 58	+40 53 07	317

The results for the first three of the seven fields in the VSA1, VSA2 and VSA3 regions (fields E, F and G) were published earlier (Grainge et al. 2003; Slosar et al. 2003). In this paper, we extend these regions (VSA1, VSA2 and VSA3) with a further four pointings per region (H, J, K and L) plus a further four new regions (VSA5, VSA6, VSA7 and VSA8) each with three pointings (E, F and G). This corresponds to a factor of $\sim$4 in the amount of extended array data and a significant increase in sensitivity over the previous results. Furthermore, the increase in sky coverage and mosaicing in each field allows an improvement in ℓ resolution, or equivalently reduced bin–bin correlations, using mosaicing techniques (Section 5.2).

3.2 Data reduction pipeline

The data reduction and calibration procedures are similar to those used for the compact array data (Paper II). Each observation is analysed individually using the REDUCE package written specifically for the VSA. The data reduction procedure is now highly developed;

much of the correcting, flagging, filtering and reweighting of the data are performed automatically. This results in data that are often close to the quality and sensitivity required for power spectrum estimation. We did however, identify residual atmospheric contamination, which was not fully accounted for by the standard routines. Such low-level emission can easily be overlooked once stacked into large data sets with mostly good quality data. Fortunately, interferometers are much less sensitive to such signals than total-power instruments, because they resolve out large angular scale emission as a result of incomplete u, v coverage at low spatial frequencies. The automatic routines dealt with correlated emission either by discarding or down-weighting of noisy or contaminated data. Nevertheless, in a few rare instances, some low-level contamination still remained. They were initially detected by non-Gaussianity tests (Section 3.5), which are very sensitive to such signals. We found that the best way to identify low-level contaminated data was to examine the raw data by eye with no smoothing or calibration applied. Once they were identified, we could remove all residual atmospheric emission or other non-astronomical signals to well below the noise on time-scales of a few seconds. The contribution therefore to the overall data set is negligible. We also searched for noise correlations introduced by such emission. We show that such bias is negligible in Section 3.5.

We continue to use Fourier filtering to remove the majority of local correlated signals including the so-called spurious signal described in Paper I. The longer baselines and larger horns of the extended array have significantly reduced this problem. The filtering removes typically 10–20 per cent of the data. The same fringe-rate filtering technique is also applied to the Sun or the Moon. Data are filtered if the Sun and the Moon are within 27° and 18° respectively, while if the Sun or the Moon are within 9° of the field centre then the entire observation is flagged. No residual Sun or Moon contamination was detected after stacking the data typically integrated over 50–100 d. The data are then further smoothed by a factor of 4 to give 64-s samples and a correction (discussed in Section 3.3) is applied for the atmospheric opacity, which is typically a few per cent at hour angles of $\sim$2.5 h.

The final step for each observation is the reweighting of the data based on the rms noise of each baseline. This is important since the noise figures can vary substantially between baselines. The reweighting also allows the optimum overall noise level to be achieved. The data are then stacked together either in hour angle, or in the u, v plane, to reduce the noise level and to facilitate further flagging of any remaining low-level bad data. Various consistency checks are performed, to verify the quality of data reduction: these are discussed in Section 3.5. Each VSA field contains $\sim 10^6$ visibilities, each of 64 s integration, which are used directly to make maps (Section 5.1). For power spectrum estimation (Section 5.2), the data are binned in the u, v plane to reduce the number of data points. Each visibility has an associated weight calculated by the reduction pipeline by accounting for integration times, flagging and noise. The reliability of these weights is verified by comparing them with those calculated from the data themselves based on the scatter in each u, v cell containing several independent 64-s samples. Both approaches gave results consistent to within a few per cent. The long-term noise characteristics of the data are agree very well with the short-term estimates from individual visibilities.

3.3 Amplitude and phase calibration

Calibration of VSA data can be split into four parts; geometric, amplitude, phase and atmospheric calibrations. The first stage is to calculate the exact geometry of the array. This requires knowledge of the x, y, z positions for each horn accurate to $\lesssim$0.1 mm. This also requires calculating the other telescope parameters [including amplitudes, phases and the mean intermediate frequency (IF)] to converge on the correct geometry, a total of $\sim$400 parameters. We use a maximum-likelihood method developed specifically for interferometric arrays, introduced by Maisinger et al. (2003). The geometry is recalculated from several long observations of Tau A each time the array is modified. Thorough testing of the geometry is made by calibrating observations of other bright radio sources.

Table 3. Calibrator sources used for amplitude and phase calibration. The absolute temperature scale is tied to a Jupiter brightness temperature of 146.6 ± 2.0 K at 33.0 GHz. Flux density spectral indices are in the convention $S \propto \nu^{-\alpha}$.

Source	RA/Dec. (J2000)	Flux density (Jy)/ temperature (K)	Spectral index α
Tau A	$05^{\rm h}35^{\rm m} + 22°01'$	333 Jy (34 GHz)	+0.30
Cas A	$23^{\rm h}23^{\rm m} + 58°49'$	168 Jy (34 GHz)	+0.83
Jupiter	–	146.6 K (33 GHz)	−2.24

Amplitude and phase corrections are calculated from a single calibrator for each of the 91 complex channels (baselines). An unresolved, non-variable bright radio source allows the measured fringes to be corrected for amplitude and phase. Table 3 lists the primary calibration sources used by the VSA with their assumed flux density S (Jy), or brightness temperature (K) and flux density spectral index, α. Note that we adopt the convention $S \propto \nu^{-\alpha}$ for the flux density spectral index. The absolute calibration from correlator units to flux density units (Jy) is described in Section 3.4. The increased flux sensitivity of the extended array, compared with the compact array, means that calibrations are reliable even for short (<1 h) observations. By cross-calibrating various bright radio sources with other sources, with no model fitting, self-calibration or other post-processing techniques, we found that the majority of VSA visibility data have phases errors less than $\sim$10°. We tested secondary (antenna-based) corrections based on calibrations made at the beginning and end of each observation. If necessary, this can correct for phase drifts during long observations. However, in general, no correction was required because the VSA typically remained phase stable for periods of several days as demonstrated in Paper I. Uncorrelated phase errors of $\sim$10° on individual visibilities have a negligible effect on CMB data because they tend to average to zero when combining a large number of visibilities. Also, the relatively low signal-to-noise ratios in the visibility data means that moderate phase errors ($\sim$10° or more) can be tolerated because we require a relatively low dynamic range.

Data recorded before 2002 July 17 were taken at a frequency of 34 GHz. As a result of a technical problem, we replaced the tunable local oscillator (LO) with a fixed frequency quartz LO. This resulted in a new centre frequency of 33.0 GHz for data taken after this change-over. For the most part, this step in frequency has little effect on the data as a whole. Nevertheless, fields observed during the frequency change were reduced and stacked separately to test for any possible systematic effects introduced by the frequency change. No significant discrepancies were found (Section 3.5).

Finally, changes in system temperature and in atmospheric opacity with elevation are corrected, based on the monitoring of modulated noise signals injected into the VSA system. Each antenna has its own noise diode to monitor changes in gain or $T_{\rm sys}$ for each antenna. This is particularly useful for identifying periods of bad weather and other problems with individual antennae. The

correction is typically a few per cent. Observations with large correction factors (>20 per cent), usually caused by bad weather or warm receivers, are discarded.

3.4 Absolute flux calibration

The absolute flux calibration of VSA data is determined from observations of Jupiter assuming a brightness temperature, $T_{\rm Jup}$. Earlier VSA results assumed $T_{\rm Jup} = 152 \pm 5$ K (3 per cent accuracy in temperature) at 32 GHz, as reported in Mason et al. (1999). The recent 1-yr *WMAP* data (Bennett et al. 2003a) are scaled to their own measurement of the CMB dipole with an accuracy of 0.5 per cent (Hinshaw 2003b). Page et al. (2003) have measured Jupiter to be $T_{\rm Jup} = 146.6 \pm 2.0$ K at 33.0 GHz corresponding to an accuracy of 1.5 per cent in temperature terms, or equivalently 3 per cent in the CMB power spectrum (ΔT^2). Note that the *WMAP* error for $T_{\rm Jup}$ is dominated by beam shape uncertainties in the *WMAP* 1-yr analysis.

We have used the new *WMAP* temperature for Jupiter as the basis for our absolute temperature scale (Table 3). In principle, this reduces the VSA calibration error in the power spectrum from 7 to 3 per cent. Indeed, the new value is consistent with the Mason et al. (1999) value at the 1σ level. However, it corresponds to a considerable 8 per cent reduction in the VSA power spectrum values compared with previous VSA data. With that in mind, we also calculated the flux density of Tau A and Cas A from the 1-yr *WMAP* data. The flux density values obtained from *WMAP* alone were found to be $\approx$4 per cent lower than those using the original VSA value in good agreement with the new calibration. Earlier VSA power spectrum measurements should therefore be scaled by a factor of 0.92 to be consistent with the new calibration scheme used here. A recent paper describing new CMB results from the CBI (Readhead et al. 2004) derived a similar scaling factor of 0.94 for their data, based on the Jupiter temperature from *WMAP*.

With angular extents of $\sim$5 arcmin, both Tau A and Cas A are partially resolved by up to $\approx$15 per cent on the longest baselines in the extended array. To correct for this, we used higher resolution maps, made at different wavelengths, as a basis of a model. For Cas A, we used 32-GHz data taken with the 100-m Effelsberg telescope (Reich, private communication). For Tau A, a 1.4-GHz map made with the VLA (Bietenholz, Frail & Hester 2001) was used and verified with a 850-μm map from the SCUBA instrument (Green 2002). We adopt the flux density spectral indices given from Mason et al. (1999; Table 3) to extrapolate between the frequencies. In a few rare instances, we also used Cyg A (33.2 Jy at 34 GHz), Saturn ($T = 135.4$ K at 32 GHz) or Venus ($T = 442.6$ K at 32 GHz).

3.5 Data checks

The VSA data are checked in a number of ways to ensure that the data are reduced correctly and that there are no systematics or contamination of the data. The usual checks consist of (i) inspecting the data by eye, (ii) parallel and independent data reduction, (iii) stacking the data in different ways, (iv) data splits, (v) simulations and (vi) a variety of tests to search for residual non-Gaussianity.

The data from each observation are displayed and examined for contaminating signals such as correlated emission from atmospheric water clouds unresolved by the telescope beam. The worst periods of bad weather are easily identified by an increase in system temperature and overall noise figures. However, unresolved clouds can result in correlated visibilities without a noticeable increase in system temperature. We found that in a small portion of the data, correlated emission remained (Section 3.2). Although such data made little difference to the final noise level, there is a concern of introducing noise correlations that could affect the power spectrum in a biased fashion. Both the reduction software and the power spectrum estimate software (Section 5.2) can deal with the full noise covariance matrix, but we assume that the off-diagonal elements were negligible to speed up the calculation of the power spectrum. We tested this assumption by calculating the non-diagonal elements of the full noise covariance matrix. On typical days, the raw data are consistent with having zero correlations in the noise. We found that on the worst affected data, the automatic routines (weighting, filtering, atmospheric calibration and reweighting) reduced the correlations to a very large degree. The off-diagonal elements were found to be negligible in virtually all cases. It is worth noting, that even if non-zero off-diagonal terms remain, they will tend to average away to zero as a result of their complex (real and imaginary) nature, as more days of data are combined. A further test was to compare the rms level well outside the primary beam with that computed for an auto-subtracted map (which is free from CMB or any other correlated signal; see Paper II). We found that the noise is indeed uncorrelated from visibility to visibility, which assures us that the noise really is decreasing with the square root of time.

The reduced data are stacked and combined in a variety of ways to look for possible contamination or other instrumental affects. By stacking the complete data set in hour angle, for a given field, any spurious signals (see Paper II) that had not been filtered out, would add coherently for each baseline and were therefore easy to detect and flag. For the extended array, very few instances of this effect were seen. In addition, the real and imaginary components of the visibility stacks were inspected in the u, v plane.

We note that where possible, the data are reduced in parallel, by at least two of the three institutions in the VSA collaboration, in order to perform consistency checking. We compared the fields analysed independently by different institutions to check that there were no major data reduction issues as a result of variations in cut-off levels, filtering parameters and subjective flagging of the data. No significant differences were found. The same comparisons were made in the power spectra, which were also found to be completely consistent with each other.

As an additional check on data consistency, the data for each VSA field were split by epoch and the χ^2 statistic was computed. Because the sky signal is the same in both halves of the data, the χ^2 statistic can be used to test for the presence of systematic errors. Table 4 gives the χ^2 values and associated significances. The term significance in this context represents the probability of exceeding the observed χ^2 value in the cumulative distribution function. For each field, and averaged over all fields, the reduced χ^2 is $\sim$1 with a combined significance of 0.50. This indicates that the splits are statistically consistent with each other. A wide range of non-Gaussianity tests were performed on individual observations and on the stacks. The techniques and results from earlier analyses are presented in Savage et al. (2004) and Smith et al. (2004). Detections of non-Gaussianity in the final stacked data were traced to a small portion of the data and hence cannot be cosmological in origin. These data were excised before calculating the final power spectrum in Section 5.2.

4 FOREGROUNDS

4.1 Source subtraction

4.1.1 Observational strategy

Discrete sources are the largest foreground for the VSA. The power spectrum of Poisson-distributed sources increases as ℓ^2 (Taylor

Table 4. The χ^2 values for data splits on each of the VSA fields. In each case the visibility data from each field were split in two according to epoch and the χ^2 of the difference vectors formed. Also tabulated are the number of degrees of freedom (d.o.f.) and the significance of each χ^2 value (see text). Fields that straddle the observing frequency change-over date are separated into 34 GHz (A) and 33 GHz (B) stacks.

Field	d.o.f.	χ^2	Significance
VSA1E	4778	4851	0.23
VSA1F	3871	3964	0.14
VSA1G	4070	3752	0.99
VSA1H_A	3867	3790	0.81
VSA1H_B	3655	3800	0.04
VSA1J	3845	3890	0.30
VSA1K	3706	3691	0.56
VSA1L	3742	3733	0.54
VSA2E	5002	5170	0.05
VSA2F	3831	3763	0.78
VSA2G	4314	4297	0.58
VSA2H	4142	4052	0.84
VSA2J_A	4120	4161	0.32
VSA2J_B	3963	4142	0.02
VSA2K	3827	3731	0.86
VSA2L	3820	3996	0.02
VSA3E	4937	5011	0.22
VSA3F	4300	4325	0.39
VSA3G	4970	5060	0.18
VSA3H_A	4236	4252	0.42
VSA3H_B	3926	3892	0.64
VSA3J	4105	4081	0.60
VSA3K	3965	4009	0.31
VSA3L	4354	4338	0.56
VSA5E	3692	3427	0.99
VSA5F	1627	1651	0.33
VSA5G	3271	4762	0.00
VSA6E_A	701	669	0.80
VSA6E_B	1297	1279	0.63
VSA6F	3578	3507	0.80
VSA6G	2085	2119	0.29
VSA7E_A	711	716	0.43
VSA7E_B	2623	2572	0.75
VSA7F	3560	3532	0.63
VSA7G	3625	3639	0.43
VSA8E_A	3039	3015	0.62
VSA8E_B	1827	1796	0.69
VSA8F	2003	1986	0.60
VSA8G	3983	4064	0.18
		Mean =	0.50

et al. 2001) while that of the CMB decreases exponentially with increasing ℓ. The point-source contribution will therefore dominate at higher ℓ values in the absence of an effective source-subtraction strategy. We carefully choose regions of the sky to not contain bright ($\gtrsim$ 500 mJy at 1.4 GHz) radio sources (Section 3.1) when extrapolated to 33 GHz from NVSS (1.4 GHz) and GB6 (4.85 GHz) catalogues. However, the contamination from sources below ∼500 mJy is still significant, particularly at the highest ℓ values.

To correct for any sources unidentified in the above surveys, the VSA employs a unique two-stage source-subtraction strategy. The first stage is to survey the regions observed by the VSA with the Ryle telescope at 15 GHz to a limiting flux density of ∼10 mJy (Waldram et al. 2003). This limit was chosen primarily to make sure that all sources that could potentially contaminate VSA data are located, even if they have rising spectra, $\alpha < 0$, between 15 and 30 GHz. Only the very steepest inverted spectrum ($\alpha < -1$) sources will be missed using this technique. The results from the recent 9C survey (fig. 9 in Waldram et al. 2003), from the Ryle telescope at 15 GHz and a completeness limit of 25 mJy, indicate that less than 1 per cent of their radio sources have $\alpha < -1$. We therefore expect little or no effect from such a rare population of sources at these flux density levels. The second stage, is to follow-up these sources with a single-baseline interferometer at the same frequency as the VSA and at the same epoch; each source is observed many times with an interval of a few days. The source-subtraction interferometer consists of two 3.7-m dishes with a 9-m N–S separation corresponding to a resolution of ∼3 arcmin and has a sensitivity of ≈340 mJy $s^{-1/2}$. The dishes are located in separate identical enclosures to minimize ground spill-over and cross-talk.

4.1.2 Source-subtractor observations and data reduction

For a typical observation, the drive system of the source subtractor takes the coordinates of the previously identified 15-GHz sources within a radius of ∼2° of the VSA field centre. A different subset (typically ∼30) of these sources is monitored over the course of each ∼5-h observing run. In this manner, the flux density of the sources is sampled over the course of the observations of a given field. This takes into account source variability on time-scales longer than a few days.

The single-baseline interferometer has identical back-end hardware to that of the main array and the data are processed in a similar way. The primary flux calibrator for the source subtractor is the planetary nebula NGC 7027. We assume a flux density of (5.45 ± 0.20) Jy at 32.0 GHz and a spectral index $\alpha = 0.1 \pm 0.1$ (Mason et al. 1999), corresponding to a ∼4 per cent calibration uncertainty. Variability of NGC 7027 is below 3 per cent (Peng et al. 2000) at VSA frequencies, apart from a secular decrease with time of ∼0.6 per cent per year (Ott et al. 1994). Phase calibration is provided by interleaved observations of the brightest sources ($\gtrsim$100 mJy) in each field.

4.1.3 Results

The result of the source monitoring programme is twofold. First, the 33 GHz flux densities of the sources in the VSA fields are known (at the time of the main array observation) and are subtracted from the visibility data down to a level of 20 mJy. The details of the complete source survey will be presented by Cleary et al. (in preparation). Secondly, the source counts derived from the observations can be used to apply a statistical correction resulting from fainter sources below the subtraction limit. This analysis assumes that the contribution from clustered sources is negligible compared with that from the Poisson component. This is a reasonable assumption on the basis of estimates for the *Planck* 30-GHz channel by Toffolatti et al. (1998).

Source monitoring for VSA source subtraction was performed at 34 and 33 GHz. In order to derive the source counts, the flux density of each source measured at 34 GHz was corrected to 33 GHz using its $\alpha^{34}_{15.2}$ spectral index. An average was then taken of the source measurements over the entire period of extended array observations. Of the 453 sources monitored, 131 were found to be >20 mJy at 33 GHz.

The 33-GHz source counts at flux densities less than ∼5 mJy are unknown; however, the counts are expected to flatten with decreasing flux density. Hence, simply extrapolating the measured

VSA source counts to fainter fluxes would overestimate the residual source contribution. In the absence of low flux density data, the measured VSA source counts were used to rescale the Toffolatti et al. (1998) 33-GHz differential source count model. Integrating the rescaled model up to 20 mJy, we get an estimate of the contribution from faint sources below the source-subtraction limit. The residual source power spectrum ($\sim$210 μK^2 at $\ell = 1000$) is then binned using the VSA window functions and directly subtracted from the bandpower estimates as an uncorrelated statistical correction. The correction applied to these data is $\Delta T^2_{\rm src} = 210(\ell/1000)^2$ in units of μK^2.

4.2 Galactic foregrounds

4.2.1 Overview

At frequencies of $\sim$30 GHz, particularly at large angular scales ($\ell < 100$), emission from the Galaxy can contaminate CMB data (Banday et al. 2003; Bennett et al. 2003b). There are currently three well-established diffuse Galactic foregrounds: synchrotron emission from relativistic electrons spiralling in the Galactic magnetic field, free–free (thermal bremsstrahlung) emission from ionized gas and vibrational dust emission. The power spectrum of Galactic emission falls with increasing ℓ (for example, see Giardino et al. 2001) and hence it is not expected to be a major contaminant at smaller angular scales. The VSA is insensitive to large angular scales ($\gtrsim 1^\circ$) as a result of the incomplete u, v coverage and primary beam attenuation. Furthermore, the VSA fields have been carefully selected to be located in cold areas of sky (Section 3.1), at high Galactic latitudes, thus minimizing any potential contamination from the Galaxy. There is however, evidence for another foreground component, recently nicknamed foreground X (de Oliveira-Costa et al. 2004), that has been shown to be strongly correlated with far-infrared (FIR) emission ($\lambda \sim 100$ μm) in the frequency range $\sim$10–50 GHz (Kogut et al. 1996; Leitch et al. 1997; de Oliveira-Costa et al. 2002; Mukherjee et al. 2002; Banday et al. 2003; Bennett et al. 2003b). A recent discussion on the possible origins of the anomalous emission, including spinning dust (Draine & Lazarian 1998) and magnetic dust grains (Draine & Lazarian 1999) is given by Banday et al. (2003). The 1-yr *WMAP* data also detect the dust-correlated component in the *K*, *Ka* and *Q* bands (Bennett et al. 2003b). Using the statistical distribution of derived spectral indices, they interpret this to be synchrotron emission with a relatively flat spectral index, $\beta \approx 2.5$ ($T \propto \nu^{-\beta}$), and constrain the spinning dust component to contribute less than 5 per cent to the foregrounds. They argue that the 408-MHz map is not a good template for synchrotron emission at higher frequencies ($\gtrsim$20 GHz) because it is dominated by steep spectrum synchrotron emission with $\beta \approx 2.9$. This is a contentious issue, which has already been re-examined but with no consensus on the origin of the anomalous component (e.g. Finkbeiner et al. 2002; Banday et al. 2003; Finkbeiner 2003a; Lagache 2003; Casassus et al. 2004; de Oliveira-Costa et al. 2004). There is none the less clear evidence for a dust-correlated component, at frequencies of $\sim$30 GHz, with a typical coupling coefficient to the SFD98 100-μm map of $T_{\rm b}/I_{100} \sim 10$ μK/(MJy sr^{-1}). Indeed, the VSA has observed selected dust clouds to further investigate the Galactic emissions at 33 GHz (Dickinson et al., in preparation).

4.2.2 Galactic foreground estimates

To quantify the Galactic foreground we use external templates because a spectral analysis is not possible for single-frequency data.

Table 5. Galactic dust-correlated foreground power estimates (rms) at $\ell = 1000$ for each VSA region based on the SFD98 100-μm map. We assume a correlation coefficient, between the foreground map (in units of MJy sr^{-1}) and 33 GHz brightness temperature (in units of μK), of 10 μK/(MJy sr^{-1}).

VSA region	rms power fluctuations (μK^2)
VSA 1	31.9
VSA 2	1.3
VSA 3	7.9
VSA 5	88.4
VSA 6	9.6
VSA 7	2.3
VSA 8	9.0

The template maps are (i) the 408-MHz all-sky map at a resolution of 51 arcmin (Haslam et al. 1981) for steep spectrum synchrotron, (ii) Hα data from the Wisconsin H-Alpha Mapper (WHAM) at 1° resolution (Haffner et al. 2003) for free–free emission and (iii) the 100-μm map at a resolution of 6.1 arcmin (SFD98) for dust-correlated emission. The synchrotron and free–free templates do not have adequate resolution to permit a full cross-correlation analysis, although high-resolution Hα data will be available in the near future (Dennison, private communication) from the Virginia-Tech Spectral-line Survey (VTSS; Dennison, Simonetti & Topasna 1998). We therefore calculate the rms fluctuations in each region at the resolution of 1° in a similar manner to the analysis used in Paper II using simple foreground models to convert to temperature fluctuations at 33 GHz. We use circular regions over a 4.°5 and 3.°0 diameter for the seven-field and three-field mosaics, respectively. We assume a spectral index for synchrotron of $\beta = 2.9$ and a conversion factor from Hα intensity, in units of Rayleigh (where $1R \equiv 10^6/4\pi$ photons s^{-1} m^{-2} sr^{-1}), to brightness temperature at 33.0 GHz, of 5.0 μK R^{-1} (Dickinson, Davies & Davis 2003; Finkbeiner 2003b). The rms values were negligible ($\lesssim$10 μK^2) in the VSA fields compared with the CMB fluctuations ($\gtrsim$1000 μK^2).

For the dust-correlated component, for which we have a high-resolution (6.1 arcmin) template, we smoothed the SFD98 100-μm map to 22 arcmin ($\ell \sim 1000$) and estimated the foreground levels by assuming a typical coupling coefficient between brightness temperature at 33 GHz and the 100-μm intensity of $T_{\rm b}/I_{100} = 10$ μK/(MJy sr^{-1}). The rms estimates are listed in Table 5. At $\ell = 1000$, the CMB fluctuations are at $\Delta T^2_{\rm rms} \sim 1000$ μK^2 while the rms foreground estimations are $\lesssim 10$ μK^2. Hence, for most of the VSA regions, the Galactic emission is essentially negligible unless they have an unusually large coupling coefficient ($\gtrsim 30$ μK/(MJy sr^{-1}). From the rms estimates in Table 5, the VSA1 and VSA5 regions seem to have stronger Galactic emission compared with the other fields. Nevertheless, these are still below the CMB anisotropies. Furthermore, there is no evidence of peculiarities when comparing these fields with the other VSA fields both in terms of the reconstructed maps (Section 5.1) or the power spectra of individual VSA regions discussed further in Section 6.

We also estimate the foreground power spectra in the VSA regions by simulating observations of the 100-μm map in the VSA fields based on the actual u, v positions of the visibilities and taking into account the primary beam. The resulting power spectra are well modelled by a simple power-law function in each case and

the expected fall-off in power with increasing ℓ agreed with previous analyses (SFD98), with power-law indices in the range -0.5 to -1.0. Of course, the exact scaling law depends on frequency and position on the sky. We fitted VSA data to the 100-μm template for each individual VSA field. This was difficult as a result of low signal-to-noise ratios and the relatively stronger CMB anisotropies. The fitted values were in the range 0–30 μK/(MJy sr^{-1}) but with large errors and no correction for chance alignments of the template maps and the CMB. Taking the average over all fields was very close to the canonical value of 10 μK/(MJy sr^{-1}). Because we are only interested in the overall effect in the combined power spectrum, we chose to stick with the canonical value. It was used to rescale the power spectra fits to each region and hence provide a statistical correction to the final VSA power spectrum in Section 5.2. The scatter on the derived coupling coefficients both here and from other experiments, at similar frequencies and angular scales, suggests that the overall scaling could be wrong by up to a factor of $\sim$2 at most. However, the correction is very small for these data and hence such an error would have only a minor effect at the lowest ℓ values ($\ell \lesssim 100$) where the VSA has little or no sensitivity: this is discussed further in Section 6. The statistical correction applied to the final power spectrum has the form $\Delta T^2_{\rm Gal} = 4.1 \times 10^3 \times \ell^{-0.72}$. This corresponds to 28 μK^2 at $\ell = 1000$. A more detailed analysis of Galactic foregrounds will be described in a forthcoming paper (Dickinson et al., in preparation).

4.3 Galaxy clusters foreground: the SZ effect

Galaxy clusters can be a serious contaminant for CMB observations. Large reservoirs of hot gas ($T \sim 10^7$ K) in the intracluster medium rescatter the CMB photons by inverse Compton scattering. Because the optical depth is typically $\sim$1 per cent, this creates a small distortion of the CMB frequency spectrum: the SZ effect (Zel'dovich & Sunyaev 1969; Sunyaev & Zel'dovich 1970). For frequencies below the CMB spectrum peak at 217 GHz, the SZ effect corresponds to a temperature decrement along the line of sight to the cluster. The largest clusters, at relatively low redshift ($z < 0.1$), can easily be detected by the VSA (Rusholme 2001; Lancaster et al. 2004) and hence it is crucial to avoid these when making CMB observations. Fortunately, the majority of nearby clusters have been identified by optical surveys such as the Abell catalogue (Abell 1958). The VSA regions are located away from known clusters (Section 3.1).

One potential contaminant, which we have not discussed so far, is the Poisson distributed contribution resulting from SZ effect decrements from virialized clusters at higher redshifts. For $2000 < \ell < 4000$ this is likely to have the same ℓ dependence as the point-source contribution, albeit with a lower amplitude. If normalization $\sigma_8 = 0.9$ then we estimate, using the cluster model described in Battye & Weller (2003), a confusion noise of $\approx$1 mJy beam^{-1}, well below the noise level in typical VSA maps, of $\approx$6 mJy beam^{-1}. If the excess power detected by CBI (Mason et al. 2003; Readhead et al. 2004) is a result of the SZ effect then $\sigma_8 \approx 1.1$ (Komatsu & Seljak 2002) and we estimate 2.5 mJy beam^{-1} compatible with an extrapolation of the observed power spectrum from $\ell = 3000$. In either case, the SZ effect foreground is not significant for current VSA data.

5 RESULTS

5.1 Maps

The primary goal of the VSA is to measure the CMB power spectrum over a wide range of angular scales. Sky maps also provide an important and complementary view of the data. To create maps of the CMB we used a maximum entropy method (MEM) described in Maisinger, Hobson & Lasenby (1997). The input data are the same binned visibility data used for deriving the power spectrum in Section 5.2. We chose to use the MEMUV option, which reconstructs the Fourier modes in the u, v plane; these are then Fourier transformed to make maps. To test the robustness of the map-making software, we tried a range of options with various parameters when producing the maps. We found no significant differences between these maps. The MEM algorithm is preferred over other deconvolution algorithms because it is optimized for extended emission by assuming a flat sky as a prior. The CLEAN algorithm (Högbom 1974), on the other hand, is optimized for unresolved sources, which are treated as delta functions convolved with the synthesized beam.

The MEM-based CMB maps made from VSA data in the extended array are presented in Fig. 3. Foreground radio sources have been removed as explained in Section 4.1. CMB anisotropies are clearly detected in all seven VSA regions.

The primary beam envelope of an interferometer permits a separation of the astronomical signal and the noise. Within the primary beam, the map contains both CMB and noise components while outside the primary beam, only noise remains. This is not the case for the MEM maps in Fig. 3, so we also created maps based on the CLEAN deconvolution algorithm with the IMAGR task in the AIPS package. Table 6 lists the estimates of CMB signal and thermal noise for individual VSA fields. Significant variations in the signal-to-noise ratio are evident (signal-to-noise ratio $\sim$1$-$3), primarily as a result of the varying integration times after flagging and filtering of the data. Note that the signal-to-noise ratio in the mosaiced maps (Fig. 3) is better as a result of the overlapping of the individual fields.

5.2 Power spectrum

The final visibility data are binned into square u, v cells, each nine wavelengths on a side, to oversample the data while reducing the number of data points by a factor of $\gtrsim$1000. Sources are subtracted using position and flux density information as described in Section 4.1. This results in 33 visibility files, one for each VSA pointing, each with $\sim 10^3$ data points.

The binned visibilities form the basic input to the maximum likelihood analysis for the CMB power spectrum. We used the Microwave Anisotropy Dataset Computational sOftWare (MADCOW) described by Hobson & Maisinger (2002).

The main binning of the VSA data reduction was chosen to Nyquist sample and to approximately match the expected phase of the peaks and troughs in the power spectrum as closely as possible. This means that there is a bin corresponding to the ℓ value expected for each peak in the power spectrum and an additional bin between the peaks. Note that this approach does not bias the parameter estimation towards the concordance model (see for example, Kuo et al. 2004): it merely acts as a matched filter that tries to extract maximum information from the fluctuations in the power spectrum. The bin positions and widths are the same as those used in Grainge et al. (2003). The considerably larger contiguous sky area in the seven field mosaics results in reduced correlation between adjacent bins. The inverse correlation matrix for the combined VSA data set is given in Table 7. The window functions are calculated as described in Paper III and are plotted in Fig. 4: they are well-fitted by Gaussian functions. In principle, finer binning is possible but at the cost of increasing the correlations and reducing the signal-to-noise ratio.

The final bandpowers calculated from the complete VSA data set, including both the compact and extended array data sets, are

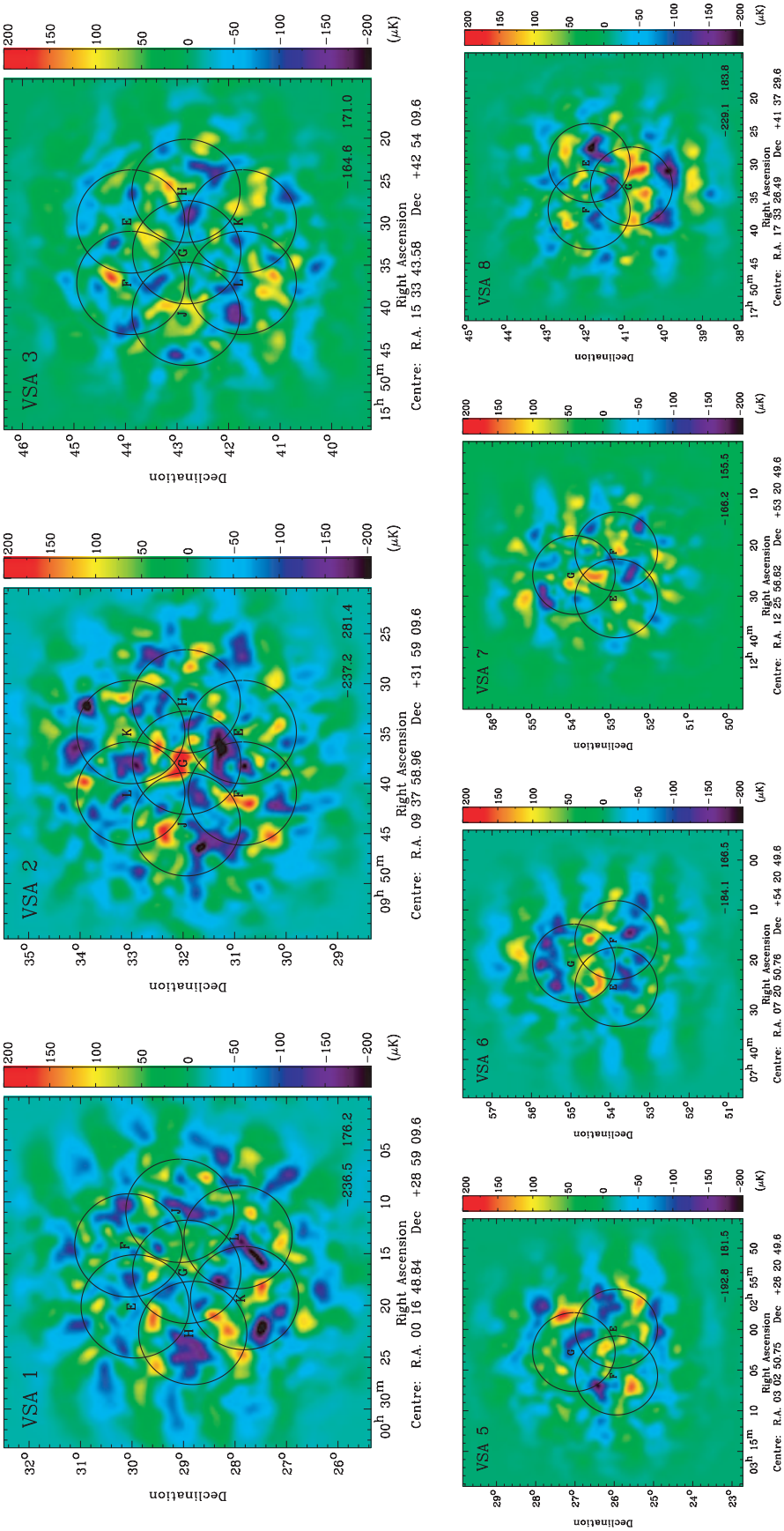

Figure 3. VSA maps of seven regions of sky (B1950 coordinates) at a resolution of ∼11 arcmin. The mosaiced maps have been deconvolved using an MEM algorithm (see text for details). VSA1, VSA2 and VSA3 are seven-field mosaics (top-row) while VSA5, VSA6, VSA7 and VSA8 are three-field mosaics (bottom row). The FWHM (≈2°) of the primary beams of each field are shown as circles. The MEM technique attenuates both signal and noise outside of the primary beams. The colour scale is fixed between −200 and +200 μK. The minimum and maximum temperatures (μK) in each mosaiced image are printed in the bottom right-hand corner of each map. The noise level varies in each field, with typical rms values of 5–25 μK beam^{-1} at the centres of the maps.

Table 6. Comparison of rms of the signal and thermal noise, all units mJy beam^{-1}, for each VSA field, measured from the CLEANed maps. The rms noise level in the centre of each map and the corresponding residual CMB signal observed in each field are given. Fields with two values (A and B) are for data at two frequencies (34 and 33 GHz, respectively).

Field	Thermal noise (rms)	rms in centre of map	CMB signal (rms)
VSA1E	8.0	18.6	16.8
VSA1F	6.9	13.8	12.0
VSA1G	8.4	11.2	7.4
VSA1H_A	9.7	13.8	9.8
VSA1H_B	7.9	14.7	12.4
VSA1J	5.2	13.5	12.5
VSA1K	6.0	20.1	19.2
VSA1L	4.2	11.6	10.8
VSA2E	8.9	16.5	13.9
VSA2F	9.6	18.2	15.5
VSA2G	7.1	22.5	21.3
VSA2H	4.8	11.9	10.9
VSA2J_A	11.0	18.3	14.6
VSA2J_B	7.8	18.5	16.8
VSA2K	6.6	17.3	16.0
VSA2L	6.2	12.6	11.0
VSA3E	7.8	15.9	13.8
VSA3F	7.7	18.4	16.7
VSA3G	6.5	12.4	10.5
VSA3H_A	8.7	18.9	16.8
VSA3H_B	9.2	14.2	10.8
VSA3J	6.8	9.0	5.9
VSA3K	6.9	12.3	10.2
VSA3L	5.1	11.4	10.2
VSA5E	6.7	9.0	6.0
VSA5F	8.0	16.4	14.3
VSA5G	5.9	13.0	11.6
VSA6E_A	10.6	10.7	1.5
VSA6E_B	8.6	14.0	11.0
VSA6F	6.7	16.4	15.0
VSA6G	7.0	9.2	6.0
VSA7E_A	8.3	7.0	–
VSA7E_B	9.2	9.7	3.1
VSA7F	5.4	14.1	13.0
VSA7G	6.1	13.8	12.4
VSA8E_A	5.9	14.2	12.9
VSA8E_B	16.0	13.5	-
VSA8F	3.8	7.3	6.2
VSA8G	5.3	14.8	13.8

listed in Table 8 for two independent binnings.[2] The final combined VSA power spectrum is presented in Fig. 5. Bright foreground sources (Section 4.1) have been subtracted from the visibility data before power spectrum estimation. The small corrections for residual sources (Section 4.1.3) and diffuse foregrounds (Section 4.2.2) have been applied and are also plotted in Fig. 5. The error bars were calculated from the probability likelihood functions by enclosing 68 per cent of the area centred on ℓ_h, the weighted median ℓ value for each bin. Calibration uncertainty (3 per cent; Section 3.4) is not included. Sample variance is included in the error estimates. Note that the extended array data have little sensitivity at $\ell \lesssim 300$ and hence the first three bins come mainly from data taken in the compact array described in Paper III.

[2] The VSA data are available at http://www.jb.man.ac.uk/research/vsa/vsa_results.html

Table 7. The correlation matrix $\mathcal{C}_{i,j}$ for the combined VSA data (main binning only), normalized to 1.0. The values of the matrix for which $\mathcal{C}_{i,j}$ is not reported, can be assumed to be zero. The final column gives the diagonal elements of the covariance matrix in units of $10^5 \times \mu K^4$.

B	$\mathcal{C}_{B,B-2}$	$\mathcal{C}_{B,B-1}$	$\mathcal{C}_{B,B}$	$\mathcal{C}_{B,B+1}$	$\mathcal{C}_{B,B+2}$	$\mathrm{Cov}_{B,B}$
1			1.0	−0.165	0.022	15.431
2		−0.165	1.0	−0.255	0.008	12.82
3	0.022	−0.255	1.0	−0.126	0.001	8.024
4	0.008	−0.126	1.0	−0.198	0.02	1.786
5	0.001	−0.198	1.0	−0.209	0.039	0.573
6	0.02	−0.209	1.0	−0.251	0.074	1.687
7	0.039	−0.251	1.0	−0.324	0.084	1.244
8	0.074	−0.324	1.0	−0.315	0.11	1.355
9	0.084	−0.315	1.0	−0.402	0.09	1.282
10	0.11	−0.402	1.0	−0.275	0.036	1.879
11	0.09	−0.275	1.0	−0.133	0.023	0.854
12	0.036	−0.133	1.0	−0.187	0.026	0.846
13	0.023	−0.187	1.0	−0.173	0.019	0.79
14	0.026	−0.173	1.0	−0.117	0.018	0.706
15	0.019	−0.117	1.0	−0.157		1.255
16	0.018	−0.157	1.0			4.261

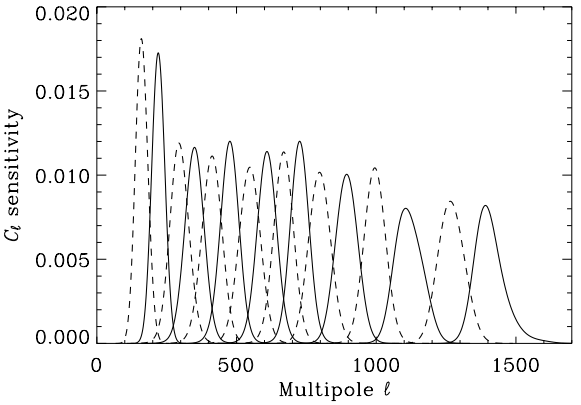

Figure 4. VSA window functions plotted as a function of ℓ for the main binning. Each curve is a single bin out of a total of 16 bins. Curves are solid and dashed lines for clarity. The window functions are, in general, well modelled by Gaussian functions.

The VSA data are also plotted in Fig. 6 along with recent data from other CMB experiments: *WMAP* (Bennett et al. 2003a), the Arcminute Bolometer Array (ACBAR; Kuo et al. 2004) and CBI (Readhead et al. 2004). Only a single binning of the data shown. No corrections are made to the external measurements for the binning schemes: they are plotted directly. Nevertheless, the overall consistency between these experiments is remarkable.

5.3 Morphological power spectrum analysis

The shape of the power spectrum was analysed following the technique described in Ödman et al. (2003). By fitting multiple Gaussians, it calculates the best fit to the data. Each Gaussian is defined by its amplitude in temperature ΔT, centre multipole ℓ and width σ.

The data were split into subsets according to the nature of each experiment. The low-frequency (LF) subset consists of the Degree Angular Scale Interferometer (DASI) (Halverson et al. 2002), CBI (Mason et al. 2003; Pearson et al. 2003) and VSA data (this work),

Table 8. The CMB bandpowers (in μK^2) for main and offset binnings of the complete VSA data set combining both compact and extended array data. The quoted ℓ ranges are nominal bin limits when the window functions fall to half the peak value, while ℓ_h is the weighted median value of the relevant window function. The error bars enclose 68 per cent of the likelihood and include sample variance.

Bin	ℓ range	ℓ_h	$T_0^2\ell(\ell+1)C_\ell/2\pi\,(\mu K^2)$	
1	100 – 190	160	3626^{+1616}_{-1150}	
1A	145 – 220	190		4430^{+1424}_{-1096}
2	190 – 250	220	5561^{+1561}_{-1232}	
2A	220 – 280	251		7236^{+1506}_{-1260}
3	250 – 310	289	5131^{+1123}_{-959}	
3A	280 – 340	321		3324^{+657}_{-548}
4	310 – 370	349	2531^{+438}_{-411}	
4A	340 – 410	376		2010^{+329}_{-274}
5	370 – 450	416	1570^{+246}_{-219}	
5A	410 – 475	431		1432^{+274}_{-246}
6	450 – 500	479	1811^{+383}_{-356}	
6A	475 – 540	501		2000^{+356}_{-329}
7	500 – 580	537	2212^{+356}_{-274}	
7A	540 – 610	581		2180^{+356}_{-301}
8	580 – 640	605	1736^{+356}_{-301}	
8A	610 – 670	639		1484^{+329}_{-301}
9	640 – 700	670	1614^{+329}_{-301}	
9A	670 – 725	696		1553^{+356}_{-329}
10	700 – 750	726	1628^{+411}_{-356}	
10A	725 – 800	759		2469^{+356}_{-301}
11	750 – 850	795	2486^{+301}_{-246}	
11A	800 – 900	843		1871^{+274}_{-274}
12	850 – 950	888	1553^{+274}_{-274}	
12A	900 – 1000	948		1398^{+274}_{-274}
13	950 – 1050	1002	1135^{+274}_{-246}	
13A	1000 – 1125	1057		837^{+246}_{-246}
14	1050 – 1200	1119	677^{+274}_{-246}	
14A	1125 – 1275	1199		886^{+329}_{-301}
15	1200 – 1350	1271	937^{+356}_{-329}	
15A	1275 – 1525	1357		704^{+329}_{-383}
16	1350 – 1700	1419	758^{+657}_{-603}	

with frequencies ∼30 GHz. The high frequency (HF) subset, corresponding to frequencies of ∼100 GHz, comprises Archeops (Benoît et al. 2003), ACBAR (Kuo et al. 2004), *BOOMERanG* (Netterfield et al. 2002) and *MAXIMA* (Lee et al. 2001) data. An additional analysis on the VSA data alone was carried out to check for consistency. *WMAP* data were not included to simplify the LF and HF split.

The results of this analysis (the amplitudes and centre ℓ values for each peak in the spectrum) are in Table 9. LF data do not tightly constrain the first-peak position owing to the lack of data points at low ℓ. This appears as a double peak in the likelihood for ℓ_1 and ΔT_1. The uncertainty on the first peak does not propagate at higher multipoles where the secondary peaks are increasingly well defined. HF data provide constraints on the first, second and third peaks whereas LF data provide constraints on the second to the fifth peaks. An important aspect of this analysis is the apparent discrepancy, at $\approx 2\sigma$ level, between LF and HF data on the amplitude of the third peak. The LF data prefer a slightly higher third peak of ≈48 μK, compared with the HF data, which prefer a lower value of ≈40 μK. This feature has been noted before and mostly accounts for the high baryon fraction derived from LF data alone.

This type of model-dependent analysis is often difficult to interpret. Specifically, the fourth and fifth peaks are not real detections and are merely a consequence of how the fitting procedure accounts for the exponential drop in power as a result of the damping tail. None the less, the structure of the CMB power spectrum, at least at $\ell < 1000$, is relatively well defined. There is good agreement between this analysis and a similar one made for the 1-yr *WMAP* data on the first and second peaks (Page et al. 2003).

6 DISCUSSION

6.1 Maps

An important application of CMB maps is to look for the signature of any non-Gaussian structures that may be foregrounds or primordial in origin, such as cosmic strings, which would appear as a discontinuity on a map, or a SZ effect, which would produce a negative temperature against the CMB.

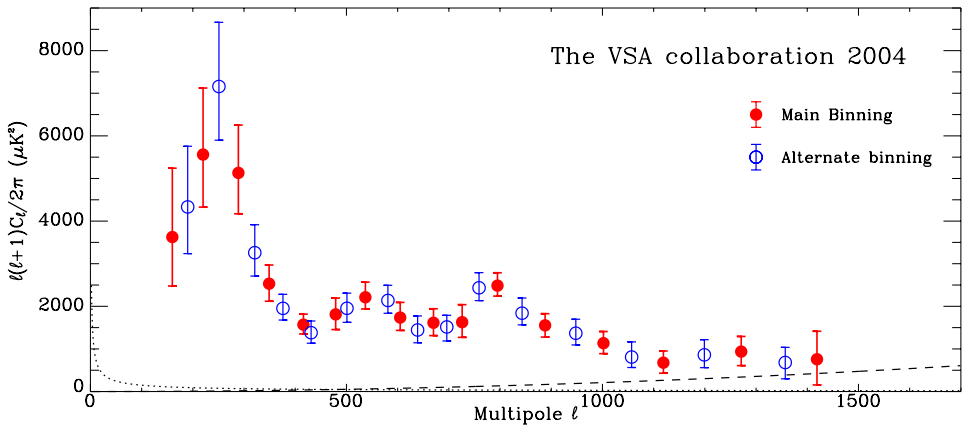

Figure 5. The CMB power spectrum as measured by the VSA by combining the extended and compact array data for all seven VSA regions. The errors represent 1σ limits from both thermal noise and sample variance. Two alternate binnings (filled and unfilled circles) are displayed (Table 8). Absolute calibration is accurate to 3 per cent and is not included in the errors. The bright radio sources have been subtracted. The smaller corrections for residual sources and Galactic foregrounds have been made and are shown as a dashed line and dotted line, respectively.

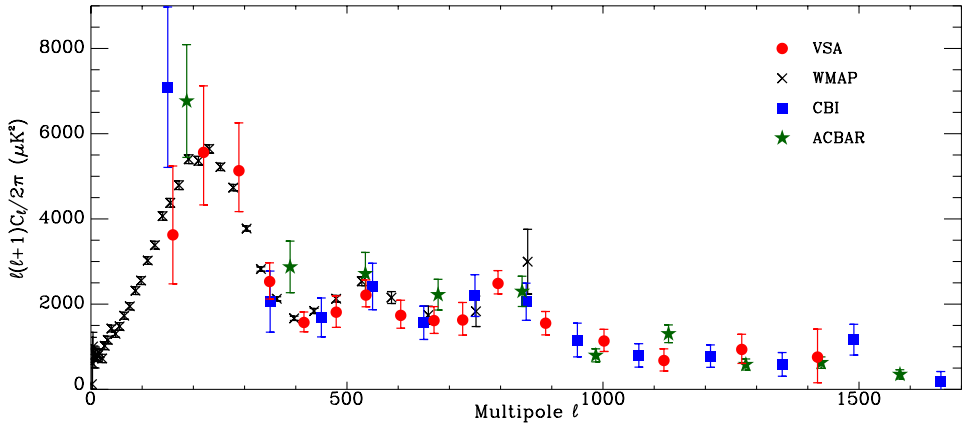

Figure 6. A comparison of the VSA data (filled circles) with those from *WMAP* 1-yr (crosses), CBI (filled squares) and ACBAR (filled stars). All errors are at the 1σ level. There is good agreement between the different experiments.

Table 9. Results of fitting Gaussians to the CMB power spectra as measured by various CMB experiments. Here we show four combinations of data (see text), including low frequency (LF; $\nu \sim 30$ GHz) and high frequency (HF; $\nu \sim 100$ GHz) data. Amplitudes are in units of μK. Errors are at the 68 per cent confidence level; nc is where there are no constraints.

parameter	Full data set	High frequency (HF)	Low frequency (LF)	VSA only
ΔT_1	$71.1^{+2.7}_{-1.9}$	$67.1^{+4.9}_{-2.3}$	$75.5^{+1.7}_{-4.7}$	$83.0^{+7.4}_{-3.4}$
ΔT_2	$43.9^{+2.0}_{-0.3}$	$42.2^{+3.0}_{-5.4}$	$43.9^{+1.4}_{-1.0}$	$47.4^{+3.6}_{-3.2}$
ΔT_3	$48.0^{+1.8}_{-1.0}$	$40.2^{+3.1}_{-3.5}$	$48.1^{+0.9}_{-3.1}$	$51.2^{+3.7}_{-6.5}$
ΔT_4	$32.3^{+0.6}_{-2.3}$	$32.0^{+7.5}_{-5.8}$	$32.0^{+1.1}_{-1.7}$	$34.9^{+2.4}_{\rm nc}$
ΔT_5	$29.6^{+2.8}_{-0.8}$	$25.2^{+7.2}_{-7.2}$	$29.0^{+2.0}_{-0.3}$	$36.8^{+2.4}_{-2.3}$
ℓ_1	217^{+2}_{-4}	214^{+4}_{-11}	$189 < \ell_1 < 236$	241^{+1}_{-8}
ℓ_2	552^{+3}_{-6}	513^{+25}_{-20}	546^{+9}_{-3}	538^{+11}_{-5}
ℓ_3	808^{+2}_{-18}	814^{+43}_{-60}	$810^{\rm nc}_{-19}$	795^{+21}_{-11}
ℓ_4	1001^{+15}_{-54}	1132^{+54}_{-78}	$969^{\rm nc}_{-41}$	988^{+31}_{-38}
ℓ_5	1322^{+12}_{-15}	1469^{+92}_{-135}	1302^{+16}_{-21}	1323^{+11}_{-22}

The largest foreground component for the VSA is discrete sources. The stronger sources can be identified in the raw VSA maps, before source subtraction. They show up as large positive temperatures in the maps, although they can coincide with negative CMB features (or noise), making faint sources difficult to identify in the sky maps. A comparison of an unsubtracted map with one that has had sources removed is presented in Fig. 7. These maps have been deconvolved with the CLEAN algorithm to optimize detection of discrete sources. In VSA6E, there are three relatively strong sources, even after correction for the primary beam attenuation, with apparent flux densities of 91, 84 and 39 mJy. The rms noise in the data is ≈10 mJy. The requirement for accurate source subtraction, as used by the VSA, is evident. The VSA maps allow a comparison to be made with other CMB data. The recent *WMAP* data release (Bennett et al. 2003a) has provided five all-sky maps at frequencies centred at 22.8 (*K* band), 33 (*Ka* band), 40.7 (*Q* band), 60.8 (*V* band) and 93.5 GHz (*W* band) with resolutions ranging from 49.2 (*K* band) to 12.6 arcmin (*W* band). The signal-to-noise ratio of *WMAP* data at the VSA resolution is ∼1 and hence much of the CMB signal is lost in the noise. The actual noise level in the *WMAP* data depends on position as a result of the scanning strategy of the *WMAP* satellite. For the 1-yr *WMAP* data release, the noise is $\sim 100 - 200$ μK per 12.6-arcmin pixel in the VSA regions, compared with ∼25 μK in the VSA mosaiced maps.

The *WMAP* team provide their own foreground-cleaned CMB maps by combining all the *WMAP* channels and optimizing the individual weights to a CMB signal. However, the resolution is constrained by the *K*-band channel at a resolution of 49 arcmin. More recently, Tegmark, de Oliveira-Costa & Hamilton (2003) have produced a foreground-cleaned CMB map at the resolution of the highest frequency channel (12.6 arcmin). In Fig. 8, we compare the VSA data for region VSA1, with the foreground-cleaned CMB map of Tegmark et al. (2003), based on *WMAP* 1-yr data at a resolution of 12.6 arcmin. The colour scale uses the same range (−200 to +200 μK) as that used in Fig. 3. Some features, both positive and negative, can be seen on both maps. The correlation is however restricted as a result of the larger noise level in the *WMAP* map for this field. The minimum and maximum values for these maps are typically ∼± 400 μK, while for the VSA maps the minimum and maximum values are ∼250 μK, in agreement with simulated CMB maps based on the concordance model and a noise level of ∼100 μK. Fig. 8 also shows the SFD98 100-μm dust map, smoothed to 11 arcmin resolution. For the VSA1 region, which contains moderate dust emission, there are no obvious Galactic signals in either the

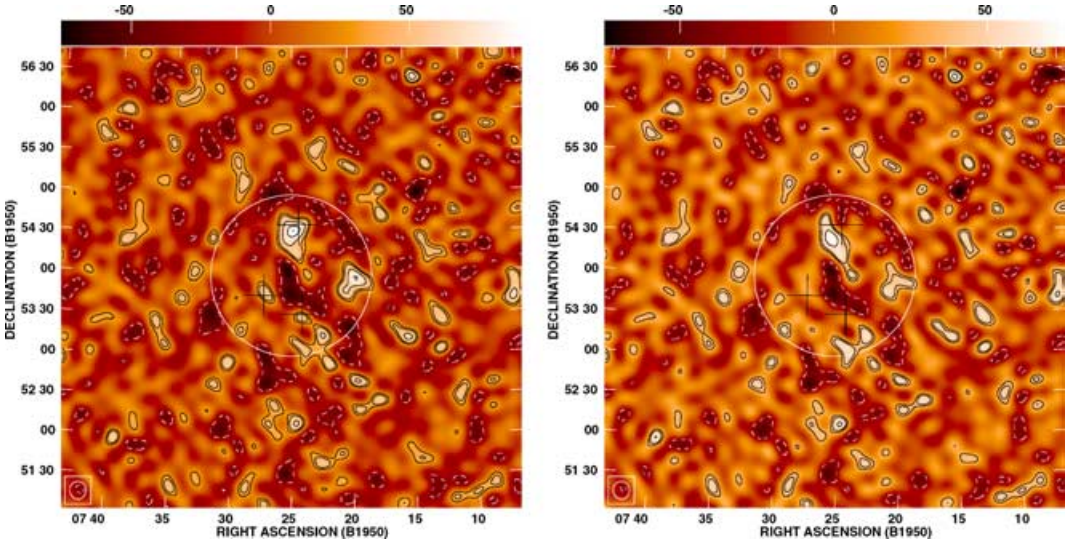

Figure 7. VSA maps of VSA6E field before and after source subtraction (Cleary 2003). The maps have been deconvolved using the CLEAN algorithm. The FWHM of the primary beam is indicated by the circle. Astronomical signals are inside the primary beam while the edges of the map, outside the primary beam, contain noise. The crosses indicate the positions of the three brightest sources in this field (see text). The rms noise level is ≈10 mJy.

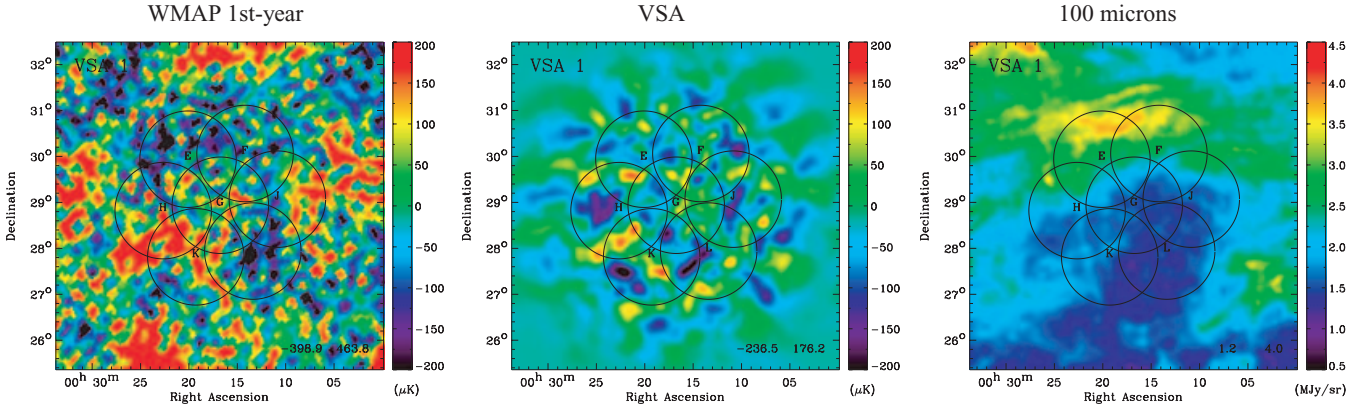

Figure 8. Comparison of maps in region VSA1. Left: Foreground-cleaned CMB map based on *WMAP* 1-yr data as reanalysed by Tegmark et al. (2003), with a resolution of 12.6 arcmin. Middle: Source-subtracted CMB map from VSA data at a resolution of ∼11 arcmin. Right: SFD98 100 μm map (in units of MJy sr^{-1}) smoothed to 11 arcmin. The *WMAP* noise level is ∼100 μK (1σ).

VSA or *WMAP* data for this region. It is evident that the strongest Galactic emissions are on large angular scales ($\ell \lesssim 100$), at least at high Galactic latitudes ($|b| \gtrsim 30^\circ$). In general, the VSA maps are consistent with each other with no obvious sign of contamination from foregrounds or other correlated signals.

6.2 Power spectrum

The VSA power spectrum (Fig. 5) clearly shows the existence of the first three acoustic peaks and the exponential fall-off in power towards higher ℓ. The *WMAP* all-sky data provides measurements limited by cosmic variance, at $\ell < 350$. At moderate to high ℓ values ($\ell \gtrsim 800$), there are fewer measurements of the CMB power spectrum. Recently, the ACBAR and CBI instruments have released new results that extend the ℓ range further. The morphological analysis presented in Section 5.3 also suggests very good agreement between experiments, particularly on the first and second peaks. The slight discrepancy in the amplitude of the third peak might suggest a change in the cosmological model. However, because the discrepancy is between LF and HF data, it is possible that this could be a consequence of some systematic effects either in the LF or HF data.

An important aspect of these results is the improved absolute calibration. We have used the *WMAP* brightness temperature for Jupiter resulting in a reduction of the VSA values by 8 per cent and an absolute uncertainty of 3 per cent in the power spectrum. Interestingly, with the new calibration scheme, the VSA data are slightly lower in amplitude, at least over the ℓ range 350–700. In fact, if we had used the original calibration scheme, we would be in closer agreement to the 1-yr *WMAP* power spectrum. We find that the best-fitting scaling factor is ≈1.05, i.e. the new VSA data are lower than the *WMAP* data by 1.6 σ.

Foregrounds in the VSA data are expected to have a negligible effect on the final power spectrum. The brighter sources have already been subtracted prior to power spectrum estimation (Section 4.1). The statistical corrections for residual sources and the Galactic foreground are relatively small as depicted in Fig. 5. Nevertheless, it is clear that the residual sources are becoming significant in the highest ℓ bins. This emphasizes the need for deeper source surveys if

we are to accurately measure CMB fluctuations at $\ell \gtrsim 1500$. On the other hand, the diffuse Galactic foregrounds are stronger at low ℓ values. In the ℓ range covered here, the foreground maps in the VSA regions suggest typical Galactic signals of a few tens of μK^2 at $\ell = 1000$ compared with the CMB at $\sim$1000 μK^2. The exception to this is VSA5 and to a lesser extent VSA1. The location of these fields (see Fig. 2) explains why the foreground estimates (Table 5) are higher than in the other fields. The diffuse foregrounds may indeed be stronger ($\sim$100 μK^2) in these fields but they still are below the CMB anisotropies ($\sim$1000 μK^2). This is verified by the fact that there are no obvious foreground signals seen either in the VSA maps or in the individual power spectra for each field. Moreover, the relative weights of the different VSA fields means that the combined power spectrum would still remain virtually unaffected: VSA5 contributes just 5 per cent to the total weight of the data as a whole. This is a major advantage of observing a number of independent fields before combining them to increase the signal-to-noise ratio in the power spectrum.

As for other systematics, the data from each individual field are tested using a Bayesian joint power spectrum and non-Gaussianity estimation discussed in Rocha et al. (2001). This method operates directly on the visibilities and, as such, is ideally suited to the detection of any residual systematics (Savage et al. 2004). Additionally, the method properly accounts for the presence of noise in the data, making it extremely sensitive to any non-Gaussian signal. However, we find no evidence of significant residual systematics in the data.

7 CONCLUSIONS

We have presented high-sensitivity and foreground subtracted measurements of the CMB power spectrum up to $\ell = 1500$ observed with the VSA. The cosmological interpretation is described in a companion paper (Rebolo et al. 2004). The final extended array data set contains a factor of $\sim$4 more than those presented by Grainge et al. (2003). The sky coverage has increased by a factor of $\sim$3 utilizing four additional three-field mosaics and increasing the original three-field mosaics to seven-field mosaics, resulting in a significant increase to the signal-to-noise ratio. Mosaicing techniques allow for smaller correlations between adjacent bins and, hence, can give finer resolution in ℓ. However, in this paper we have used the same binning scheme as Grainge et al. (2003) for comparison and to reduce the bin–bin correlations; the ℓ resolution is $\Delta\ell \approx 60$. We adopt a new absolute calibration scheme based on Jupiter temperature measurements with *WMAP* to give a 3 per cent accurate absolute scale in the power spectrum. This reduces absolute values by 4 per cent in temperature or 8 per cent in the power spectrum compared with previous VSA data.

The VSA power spectrum (Fig. 5) is in good agreement with data from other CMB experiments. There are now good signal-to-noise detections of the first three peaks in the CMB power spectrum and a damping tail at high ℓ, which continues to $\ell \sim 1500$. The different instruments have different potential systematic problems and they cover a wide range of frequencies. The agreement therefore indicates that none of the experiments is seriously contaminated by foreground emission or other systematic effects (see also Griffiths & Lineweaver 2004). From the analysis of the peak structure (Section 5.3), there is extremely good agreement on the peak structure between experiments, except for a slight discrepancy in the amplitude of the third peak, which may have important consequences for the cosmological models. The slight discrepancy ($\sim 1.6\sigma$) in the overall scaling between VSA and *WMAP* may also be an important factor in terms of fitting cosmological models. This is discussed by Rebolo et al. (2004).

In the near future, the VSA will be reconfigured with even larger horns and longer baselines. It will allow the VSA to increase the ℓ range even further, up to a maximum of $\ell \sim 3000$, while maintaining good ℓ resolution without loss of overall temperature sensitivity. The assistance of HF radio source surveys, to identify and measure the flux densities of sources over large areas of sky, will be a crucial role in keeping the discrete source foregrounds under control. The One Centimetre Receiver Array (OCRA; Browne et al. 2000), a prototype multibeam receiver system currently begin tested on the Torun 32-m telescope, will be ideal for such purposes. Moreover, OCRA is currently operating at 30 GHz and hence direct source subtraction, without the need to extrapolate to other frequencies, will be possible in the near future.

ACKNOWLEDGMENTS

First of all we thank the anonymous referee for detailed comments that have significantly improved the style of the paper and presentation of the results. CD is grateful to Tim Pearson for reading the text carefully and making useful comments on the paper. We thank the staff of Jodrell Bank Observatory, Mullard Radio Astronomy Observatory and the Teide Observatory for assistance in the day-to-day operation of the VSA. We are very grateful to PPARC for the funding and support for the VSA project and to the Instituto de Astrofísica de Canarias (IAC) for supporting and maintaining the VSA in Tenerife. Partial financial support was provided by Spanish Ministry of Science and Technology project AYA2001-1657. JARM acknowledges the hospitality of the IAC during several visits. CD acknowledges PPARC for funding a post-doctoral research associate position for part of this work. KL, NR, AS and RS are funded by PPARC studentships. YAH is supported by the Space Research Institute of KACST. AS acknowledges the support of St. Johns College, Cambridge. CO thanks the African Institute for Mathematical Sciences for their hospitality.

REFERENCES

Abell G. O., 1958, ApJS, 3, 211
Banday A. J., Dickinson C., Davies R. D., Davis R. J., Górski K. M., 2003, MNRAS, 345, 897
Battye R. A., Weller J., 2003, Phys. Rev. D, 68, 083506
Bennett C. L. et al., 2003a, ApJS, 148, 1
Bennett C. L. et al., 2003b, ApJS, 148, 97
Benoît A. et al., 2003, A&A, 399, L19
Bietenholz M. F., Frail D. A., Hester J. J., 2001, ApJ, 560, 254
Browne I. W., Mao S., Wilkinson P. N., Kus A. J., Marecki A., Birkinshaw M., 2000, inR. Harvey Butcher, ed., Proc. SPIE Vol. 4015, Radio Telescopes. Int. Soc. Opt. Eng., New York, p. 299
Casassus S., Readhead A. C. S., Pearson T. J., Nyman L.-A., Shepherd M. C., Bronfman L., 2004, ApJ, 603, 599
Cleary K., 2003, PhD thesis, Univ. Manchester
Condon J. J., Cotton W. D., Greisen E. W., Yin Q. F., Perley R. A., Taylor G. B., Broderick J. J., 1998, AJ, 115, 1693
Dawson K. S., Holzapfel W. L., Carlstrom J. E., Joy M., LaRoque S. J., Miller A. D., Nagai D., 2002, ApJ, 581, 86
Dennison B., Simonetti J. H., Topasna G. A., 1998, PASP, 15, 147
de Oliveira-Costa A. et al., 2002, ApJ, 567, 363
de Oliveira-Costa A., Tegmark M., Davies R. D., Gutiérrez C. M., Lasenby A. N., Rebolo R., Watson R. A., 2004, ApJ, 609, L89
Dickinson C., Davies R. D., Davis R. J., 2003, MNRAS, 341, 369
Draine B. T., Lazarian A., 1998, ApJ, 494, L19
Draine B. T., Lazarian A., 1999, ApJ, 512, 740

Ebeling H., Edge A. C., Böhringer H., Allen S. W., Crawford C. S., Fabian A. C., Voges W., Huchra J. P., 1998, MNRAS, 301, 881
Finkbeiner D. P., 2003a, ApJ, in press (astro-ph/0311547)
Finkbeiner D. P., 2003b, ApJS, 146, 407
Finkbeiner D. P., Schlegel D. J., Curtis F., Heiles C., 2002, ApJ, 566, 898
Giardino G., Banday A. J., Fosalba P., Górski K. M., Jonas J. L., O'Mullane W., Tauber J., 2001, A&A, 371, 708
Grainge K. J. B. et al., 2003, MNRAS, 341, L23
Green D. A., 2002, in Slane P. O., Gaensler B. M., eds, ASP Conf. Ser. Vol. 271, Neutron Stars in Supernova Remnants. Astron. Soc. Pac., San Francisco, 153
Gregory P. C., Scott W. K., Douglas K., Condon J. J., 1996, ApJS, 103, 427
Griffiths L. M., Lineweaver C. H., 2004, ApJ, 603, 371
Haffner L. M., Reynolds R. J., Tufte S. L., Madsen G. J., Jaehnig K. P., Percival J. W., 2003, ApJS, 149, 405
Halverson N. W. et al., 2002, ApJ, 568, 38
Haslam C. G. T., Klein U., Salter C. J., Stoffel H., Wilson W. E., Cleary M. N., Cooke D. J., Thomasson P., 1981, A&A, 100, 209
Hinshaw G. et al., 2003a, ApJS, 148, 135
Hinshaw G. et al., 2003b, ApJS, 148, 63
Hobson M. P., Maisinger K., 2002, MNRAS, 334, 569
Högbom J. A., 1974, A&AS, 15, 417
Kogut A., Banday A. J., Bennett C. L., Gorski K. M., Hinshaw G., Smoot G. F., Wright E. I., 1996, ApJ, 464, L5
Komatsu E., Seljak U., 2002, MNRAS, 336, 1256
Kuo C. L. et al., 2004, ApJ, 600, 32
Lagache G., 2003, A&A, 405, 813
Lancaster K. et al., 2004, MNRAS, in press (astro-ph/0405582)
Lawrence C. R., 2003, SPIE, 4850, L710
Lee A. T. et al. 2001, ApJ, 561, L1
Leitch E. M., Readhead A. C. S., Pearson T. J., Myers S. T., 1997, ApJ, 486, L23
Maisinger K., Hobson M. P., Lasenby A. N., 1997, MNRAS, 290, 313
Maisinger K., Hobson M. P., Saunders R. D. E., Grainge K. J. B., 2003, MNRAS, 345, 800
Mason B. S.Leitch E. M., Myers S. T., Cartwright J. K., Readhead A. C. S., AJ, 1999, 118, 2908
Mason B. S. et al., 2003, ApJ, 591, 540
Mukherjee P., Dennison B., Ratra B., Simonetti J. H., Ganga K., Hamilton J., 2002, ApJ, 579, 83
Netterfield C. B. et al., 2002, ApJ, 571, 604
Ödman C. J., Melchiorri A., Hobson M. P., Lasenby A. N., 2003, Phys. Rev. D, 67, 083511
Ott M., Witzel A., Quirrenbach A., Krichbaum T. P., Standke K. J., Schalinski C. J., Hummel C. A., 1994, A&A, 284, 331
Page L. et al., 2003, ApJS, 148, 39
Pearson T. J. et al., 2003, ApJ, 591, 556
Peng B., Kraus A., Krichbaum T. P., Witzel A., 2000, A&AS, 145, 1
Readhead A. C. S. et al., 2004, ApJ, 609, 498
Rebolo R. et al., 2004, MNRAS, in press (astro-ph/0402466; doi:10.1111/j.1365-2966.2004.08102.x) (this issue)
Rocha G., Magueijo J., Hobson M., Lasenby A., 2001, Phys. Rev. D, 64, 63512
Rusholme B., 2001, PhD thesis, Cambridge Univ.
Savage R. S. et al., 2004, MNRAS, 349, 973
Schlegel D. J., Finkbeiner D. P., Davis M., 1998, ApJ, 500, 525 (SFD98)
Scott P. F. et al., 2003, MNRAS, 341, 1076 (Paper III)
Slosar A. et al., 2003, MNRAS, 341, L29
Smith S. et al., 2004, MNRAS, 352, 887
Smoot G. F. et al., 1992, ApJ, 396, L1
Spergel D. N. et al., 2003, 148, 175
Sunyaev R. A., Zel'dovich Y. B., 1970, ApJS, 7, 3
Tauber J. A., 2001, in Harwitt M., Hauser M. G., eds, Proc. IAU Symp. 204, The Extragalactic Infrared Backgrounds and its Cosmological Implications. Astron. Soc. Pac., San Francisco, p. 493
Taylor A. C., Grainge K., Jones M. E., Pooley G. G., Saunders R. D. E., Waldram E. M., 2001, MNRAS, 327, L1
Taylor A. C. et al., 2003, MNRAS, 341, 1066 (Paper II)
Tegmark M., de Oliveira-Costa A., Hamilton A. J. S., 2003, Phys. Rev. D, 68, 123523
Toffolatti L., Argueso Gomez F., de Zotti G., Mazzei P., Franceschini A., Danese L., Burigana C., 1998, MNRAS, 297, 117
Waldram E. M., Pooley G. G., Grainge K. J. B., Jones M. E., Saunders R. D. E., Scott P. F., Taylor A. C., 2003, MNRAS, 342, 915
Watson R. A. et al., 2003, MNRAS, 341, 1057 (Paper I)
Zel'dovich Y. B., Sunyaev R. A., 1969, ApJS, 4, 301

This paper has been typeset from a TEX/LATEX file prepared by the author.